Diffusion imaging of reversible and irreversible microstructural changes within the corticospinal tract in idiopathic normal pressure hydrocephalus

Kouhei Kamiya[a,b,*], Masaaki Hori[b], Ryusuke Irie[a,b], Masakazu Miyajima[c], Madoka Nakajima[c], Koji Kamagata[b], Kouhei Tsuruta[b], Asami Saito[b], Misaki Nakazawa[d], Yuichi Suzuki[e], Harushi Mori[a], Akira Kunimatsu[a], Hajime Arai[c], Shigeki Aoki[b], Osamu Abe[a]

[a]Department of Radiology, The University of Tokyo, Bunkyo, Tokyo, Japan
[b]Department of Radiology, Juntendo University School of Medicine, Bunkyo, Tokyo, Japan
[c]Department of Neurosurgery, Juntendo University School of Medicine, Bunkyo, Tokyo, Japan
[d]Department of Radiological Sciences, Graduate School of Human Health Sciences, Tokyo Metropolitan University, Arakawa, Tokyo, Japan
[e]Department of Radiology, The University of Tokyo Hospital, Bunkyo, Tokyo, Japan

ARTICLE INFO

ABSTRACT

The symptoms of idiopathic normal pressure hydrocephalus (iNPH) can be improved by shunt surgery, but prediction of treatment outcome is not established. We investigated changes of the corticospinal tract (CST) in iNPH before and after shunt surgery by using diffusion microstructural imaging, which infers more specific tissue properties than conventional diffusion tensor imaging. Two biophysical models were used: neurite orientation dispersion and density imaging (NODDI) and white matter tract integrity (WMTI). In both methods, the orientational coherence within the CSTs was higher in patients than in controls, and some normalization occurred after the surgery in patients, indicating axon stretching and recovery. The estimated axon density was lower in patients than in controls but remained unchanged after the surgery, suggesting its potential as a marker for irreversible neuronal damage. In a Monte-Carlo simulation that represented model axons as undulating cylinders, both NODDI and WMTI separated the effects of axon density and undulation. Thus, diffusion MRI may distinguish between reversible and irreversible microstructural changes in iNPH. Our findings constitute a step towards a quantitative image biomarker that reflects pathological process and treatment outcomes of iNPH.

1. Introduction

Idiopathic normal pressure hydrocephalus (iNPH) is a geriatric disease characterized by the triad of gait disturbance, cognitive impairment, and urinary incontinence (Halperin et al., 2015; Mori et al., 2012). The reported prevalence is 0.51–2.9% in the elderly population (Miyajima et al., 2016). The symptoms of iNPH can be improved by surgery to create a ventriculo-peritoneal or lumbo-peritoneal cerebrospinal fluid (CSF) shunt (Kazui et al., 2015; Miyajima et al., 2016), especially in the early stage of the disease (Bradley, 2015). However, the reported degree of improvement has varied widely among different case series (Halperin et al., 2015; Poca et al., 2005; Solana et al., 2012). Therefore, a quantitative biomarker that reflects disease severity and predicts treatment response has been sought (Ringstad et al., 2016; Virhammar et al., 2014).

Diffusion MRI has revealed valuable insights into many disorders and age-related changes in the central nervous system by providing quantitative measures of neural microstructure, such as fractional anisotropy (FA), in conventional diffusion tensor imaging (DTI) (Abe et al., 2002; Cohen et al., 2017; Sexton et al., 2011; Shizukuishi et al., 2013). Generally, neurological disorders are associated with decreased FA, which has been attributed to pathologies such as white matter degeneration, demyelination, and gliosis. The FA increase within the corticospinal tract (CST) in iNPH is an interesting exception (Hattingen et al., 2010; Hattori et al., 2012; Jurcoane et al., 2014; Kim

et al., 2011; Nakanishi et al., 2013; Scheel et al., 2012). This phenomenon distinguishes iNPH from other dementia disorders. The FA increase, which is driven by the increase of axial diffusivity (AD), has been speculated to reflect the stretching of neural fibers due to compression by the enlarged ventricle. The axons undulate in the normal physiological state, and stretching (which reduces undulation) increases FA and AD (Nilsson et al., 2012). A few studies have reported that the increased FA and AD of the CST tend to normalize after shunt surgery (Jurcoane et al., 2014; Kim et al., 2011; Scheel et al., 2012), consistent with recovery from stretching.

The increased FA in the CST in iNPH contrasts with the decrease in FA in areas outside the CST in iNPH and other chronic neurological diseases (Hattori et al., 2012; Scheel et al., 2012); thus, correlating FA with symptom severity or treatment response is difficult. In a previous study, the correlation between CST FA and the severity of gait disturbance in iNPH was weak (Hattingen et al., 2010). We hypothesize that FA within the CST in iNPH reflects a mixture of an increase caused by axon stretching and a decrease caused by neurodegeneration. Although axon stretching is expected to be at least partially reversible, the existence of shunt non-responders indicates that part the neuronal damage in the chronic stage of iNPH is irreversible. Although a correlation between AD of the CST and treatment response has been reported (Jurcoane et al., 2014), relying solely on AD for predicting surgical outcomes is also difficult, because loss of neuronal cells may increase diffusivities in all directions, including AD.

Although FA and other conventional DTI measures are sensitive to many microstructural properties, such as axon density, orientational coherence, and myelination, they are not highly specific to any of these properties (Jones et al., 2013). Towards more specific quantification of brain microstructure, the trend in diffusion MRI is to develop white matter model consisting of several compartments and to estimate the compartment parameters (orientation, volume fraction, diffusivity, etc.) from the measured signals. For example, the composite hindered and restricted water diffusion (CHARMED) model (Assaf and Basser, 2005) represented the intra-cellular compartment as impermeable parallel cylinders with a gamma distribution of radii and the extra-cellular compartment as anisotropic diffusion tensor, and provided sensible maps of axon density in vivo. Subsequently, Alexander et al. introduced minimal model of white matter diffusion (MMWMD) to obtain orientationally-invariant measurement (Alexander et al., 2010). However, the long scan time had been the limitation for clinical application of these techniques. Recently, neurite orientation dispersion and density imaging (NODDI) (Zhang et al., 2012) enabled estimation of the intracellular volume fraction (v_{ic}) and orientation dispersion index (ODI) from a clinically achievable scan, and has been widely used to investigate neurological disorders and normal aging (Cercignani et al., 2017; Colgan et al., 2015; Kamagata et al., 2016; Merluzzi et al., 2016). Typically, a decrease of v_{ic} is interpreted as neuronal loss. Irie et al. reported that a decrease of ODI in the CST was more specific to iNPH than an FA increase (Irie et al., 2017). They also observed that v_{ic} of the CST was lower in patients than in controls, indicating the potential of v_{ic} as a marker of chronic damage in iNPH. In this context, we investigated the postoperative changes of these metrics in the present study. If ODI is specific to stretching and v_{ic} is specific to neuronal loss, ODI should normalize after the surgery, whereas v_{ic} should not.

Currently available methods of diffusion microstructural imaging rely on simplified models, and parameters of interest are occasionally estimated at the cost of introducing constraints that may be invalid. Among the several constraints for NODDI, the assumption of a single, fixed diffusivity for nervous tissue throughout the whole brain (for human in-vivo studies, 1.7×10^{-3} mm²/s) is especially unrealistic in disease conditions like iNPH. Although simplification is required for achieving clinical practicability in both data acquisition and analyses, we need to recognize the biases. To make our observations more convincing, we compared NODDI with another method, white matter tract integrity (WMTI) (Fieremans et al., 2011), and looked into the

consistency of the results. WMTI is not based on fixed diffusivity values, but rather estimates intra- and extra-axonal diffusivities independently. WMTI contains different assumptions and limitations from those of NODDI, as detailed in Section 2.1. Finally, neither NODDI nor WMTI explicitly takes axon undulation into account. Alteration of properties not included in the model can influence the output parameters; for example, neurite beading affects NODDI and WMTI metrics (Skinner et al., 2015). To investigate how stretching and axon density affect the estimated metrics, we carried out Monte-Carlo simulation using undulating cylinders as model of axons.

2. Materials and methods

2.1. Theory

2.1.1. The common basis of NODDI and WMTI

Both NODDI and WMTI rely on the popular overarching model that considers the intra-axonal compartment as "stick". In other words, they assume the transverse signal attenuation from the intra-axonal space to be zero. This assumption has been supported by several recent studies that reported diffusion measurement with current clinical MR systems are practically insensitive to the transverse signal attenuation from the intra-axonal space (Burcaw et al., 2015; Ning et al., 2017; Novikov et al., 2016a). As detailed in the Sections 2.1.2 and 2.1.3, NODDI and WMTI differ in how they deal with the diffusivities (fixed or estimated), the orientation distribution function (dispersed or coherent), and the number of compartments.

2.1.2. NODDI

NODDI describes the diffusion MRI signal as a sum of three non-exchanging compartments:

$$S = (1 - v_{iso})(v_{ic}S_{ic} + (1 - v_{ic})S_{ec}) + v_{iso}S_{iso} \qquad (1)$$

where S is the entire normalized signal; S_{ic}, $S_{ec,}$ and S_{iso} are the normalized signals of the intracellular, extracellular, and CSF compartments, respectively; and v_{ic} and v_{iso} are the normalized volume fractions of the intracellular and CSF compartments, respectively (Zhang et al., 2012). The intracellular, extracellular, and CSF compartments are modeled as sticks with orientation dispersion, anisotropic Gaussian diffusion (tensor ellipsoids), and isotropic Gaussian diffusion, respectively. NODDI mainly focuses on estimating dispersion and uses a single fixed diffusivity value for both intra- and extra-axonal spaces. NODDI also describes axon orientation distribution with a single Watson distribution, and approximates the extra-axonal transverse diffusivity ($D_{e,\perp}$) as a function of the intracellular volume and parallel diffusivity ($D_{e,\parallel}$, fixed as 1.7×10^{-3} mm²/s), i.e., as $D_{e,\perp} = D_{e,\parallel}(1 - v_{ic})$.

2.1.3. WMTI

The WMTI model (Fieremans et al., 2011) relates diffusional kurtosis imaging metrics (Jensen and Helpern, 2010) to features of white matter microstructure. The intra-axonal volume fraction, also known as the axonal water fraction (AWF), is calculated as:

$$AWF = \frac{K_{max}}{K_{max} + 3} \qquad (2)$$

where K_{max} is the maximum kurtosis over all possible directions. The diffusion tensors of the intra- and extra-axonal compartments are derived, with diffusion in the intra- and extra-axonal spaces given by:

$$D_{a,n} = D_n\left[1 - \sqrt{\frac{K_n(1 - AWF)}{3AWF}}\right], D_{e,n} = D_n\left[1 + \sqrt{\frac{K_n \cdot AWF}{3(1 - AWF)}}\right] \qquad (3)$$

where D_n and K_n are the diffusion and kurtosis, respectively, in a given direction n. The intra-axonal diffusivity parallel to axons (D_a) is

expressed as $D_a = \mathrm{Tr}(\widehat{D_a})$. In the extra-axonal space, the parallel (D_{epar}) and perpendicular (D_{eperp}) diffusivities are defined in an analogous fashion to axial and radial diffusivities (AD and RD) in conventional DTI. The equations assume that $D_a \leq D_e$ for every direction. WMTI is also based on the explicit assumption of straight coherent fibers, but is regarded as a good approximation for fiber dispersion of up to 30° in clinically relevant scans (Fieremans et al., 2011).

2.2. Participants

The institutional review board approved this study, and written informed consent was obtained from all participants. Ten patients with iNPH (3 males and 7 females; 75.3 ± 5.1 years old) and 14 age-matched control subjects (4 males and 10 females; 74.3 ± 3.5 years old) were involved. Diagnosis of iNPH was made according to the criteria of probable iNPH, provided by the Japanese Clinical Guidelines for Idiopathic Normal Pressure Hydrocephalus (Mori et al., 2012). Those who had a history of neurological disease other than iNPH were excluded. All patients underwent lumbo-peritoneal shunt surgery and reported subjective improvement of gait disturbance. MRI was performed before and after the surgery with the same acquisition protocol (see Section 2.3). The mean interval between the surgery and postoperative MRI was 9 months (ranging from 3 to 17 months). Normal control subjects were required to be >60 years of age and free of neurological or psychological diseases.

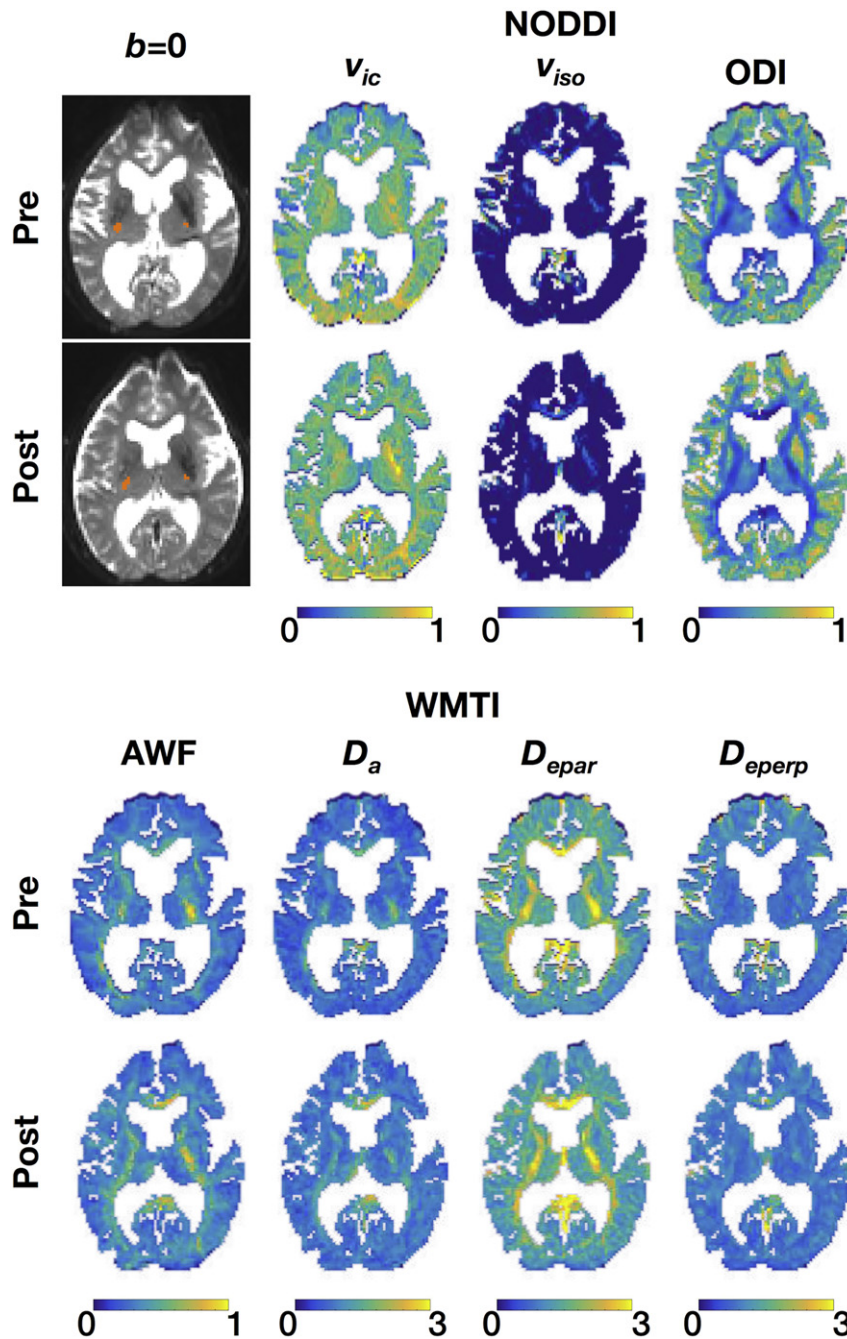Fig. 1. Examples of output maps from NODDI and WMTI. The CST tractography is superimposed on the $b = 0$ images (orange). The pre-operative images are presented in the upper row, while the post-operative images of the same individual are displayed in the lower row. For D_a, D_{epar}, and D_{eperp}, the color bar is in the unit of $\mu m^2/ms$. v_{ic}, v_{iso}, ODI, and AWF are unitless.

2.3. Image acquisition

Diffusion MRI data was acquired using a 3-T unit (Achieva, Philips Medical Systems, Best, the Netherlands), equipped with an 8-channel head coil. A single-shot, spin-echo echo planar imaging sequence was used with 5 diffusion weightings ($b = 500, 1000, 1500, 2000,$ and 2500 s/mm^2) along 32 non-collinear directions, and 1 $b = 0$ s/mm^2 volume (TR = 3000 ms; TE = 80 ms; axial slices, 20; matrix, 128 × 128; voxel size = 2 mm × 2 mm × 5 mm; parallel imaging factor, 2; half-Fourier factor, 0.667; NEX, 2; acquisition time, 824 s). The gradient length (δ) and the time between the 2 leading edges of the diffusion gradient (Δ) were held constant (Δ/δ = 39/28 ms).

2.4. Image processing

Pre-processing of diffusion data included image denoising based on random matrix theory (Veraart et al., 2016), correction for eddy currents and motions (FSL's *eddy*; (Andersson and Sotiropoulos, 2016), and correction for B1 bias field based on the $b = 0$ images using N4ITK (Tustison et al., 2010). Publicly available toolbox was used for processing NODDI (https://www.nitrc.org/projects/noddi_toolbox) (Zhang et al., 2012) and WMTI (https://github.com/NYU-DiffusionMRI/Diffusion-Kurtosis-Imaging) (Fieremans et al., 2011; Veraart et al., 2013), respectively. Examples of the output maps are shown in Fig. 1.

To make the comparison between the two models more intuitive, we translated the estimated metrics as proposed previously (Jelescu et al., 2015). From the definition of the 3 compartments in the NODDI model (Eq. [1]), AWF from NODDI is expressed as $v_{ic}(1 - v_{iso})$. For WMTI, estimation of the dispersion is represented as:

$$\tau_1 = cos^2\psi = \frac{D_{a,1}}{Tr\left(\widehat{D_a}\right)} \qquad (4)$$

where ψ is the angle of dispersion around the main axis. For NODDI, the relationship between ODI and τ_1 is expressed as:

$$ODI = \frac{2}{\pi}\arctan(1/\kappa), \tau_1 = -\frac{1}{2\kappa} + \frac{1}{\sqrt{\pi}e^{-\kappa}erfi\left(\sqrt{\kappa}\right)\sqrt{\kappa}} \qquad (5)$$

where κ is the concentration parameter of the Watson distribution (Zhang et al., 2012). τ_1 varies from 1/3 for an isotropically dispersed orientation to 1 for a strictly parallel orientation.

2.5. Image analyses

Tract-specific analysis of the CST was performed. Using tractography as a volume of interest (VOI), the tract-specific analysis is more reproducible as compared to a simple in-plane region of interest (ROI) measurement (Brandstack et al., 2016). From the $b = 0$ and $b = 1000$ s/mm^2 volumes, we reconstructed deterministic diffusion tensor tractography of the CST and maps of conventional DTI metrics (FA, MD, AD, and RD), using Diffusion Toolkit (http://www.trackvis.org/dtk/). The seed was placed in the primary motor cortex, and the target was placed in cerebral peduncle (Wakana et al., 2007). Because previous studies localized the FA increase within the CST (Hattori et al., 2012; Scheel et al., 2012), the lower and upper boundaries of the VOI were defined as the internal capsule and the superior longitudinal fasciculus, respectively (Fig. 2). We note CST tractography and calculation of the DTI metrics used only the $b = 0$ and $b = 1000$ s/mm^2 volumes for comparability with the previous studies, while newer tractography algorithms (Glenn et al., 2015; Jeurissen et al., 2014) and/or DTI metrics estimation (Veraart et al., 2011) based on multi b-value data could have been applied.

Given the lack of an a priori hypothesis regarding laterality differences, the mean value of the left and right CST was used for statistical analyses. Welch's *t*-test was performed to investigate differences between the iNPH patients and the controls. Paired *t*-tests were performed to compare pre- and post-operative values. The significance threshold was set at $p = 0.05$. For comparison with the literature, conventional DTI metrics were also analyzed.

2.6. Monte-Carlo simulation

Virtual diffusion data were generated using a Monte-Carlo random walk simulation implemented in Camino (http://camino.cs.ucl.ac.uk/) (Hall and Alexander, 2009). First, we constructed an undulating cylinder model of axons. The cylinders, which are arranged along the z direction and have diameter of 4 μm, undulate sinusoidally in the x direction (Fig. 3). The path of the axon is given by:

$$f(z) = \left[Acos\left(\frac{z}{L}2\pi\right), 0, z\right] \qquad (6)$$

where A is the undulation amplitude and L is the wavelength. In the following, the strength of undulation is represented by λ (the ratio of the path length in one wave to L) instead of A, in accordance with a previous study (Nilsson et al., 2012). λ is equal to 1 in a straight axon and increases with undulation. In this experiment, λ was varied from 1 to 1.20, with L fixed as 24 μm. The cylinders were hexagonally packed without touching, and the occupation within the space (axonal volume fraction, VF) was varied. Simulations were performed using all combinations of λ = [1, 1.05, 1.1, 1.15, 1.2], and VF = [0.4, 0.5, 0.6, 0.7].
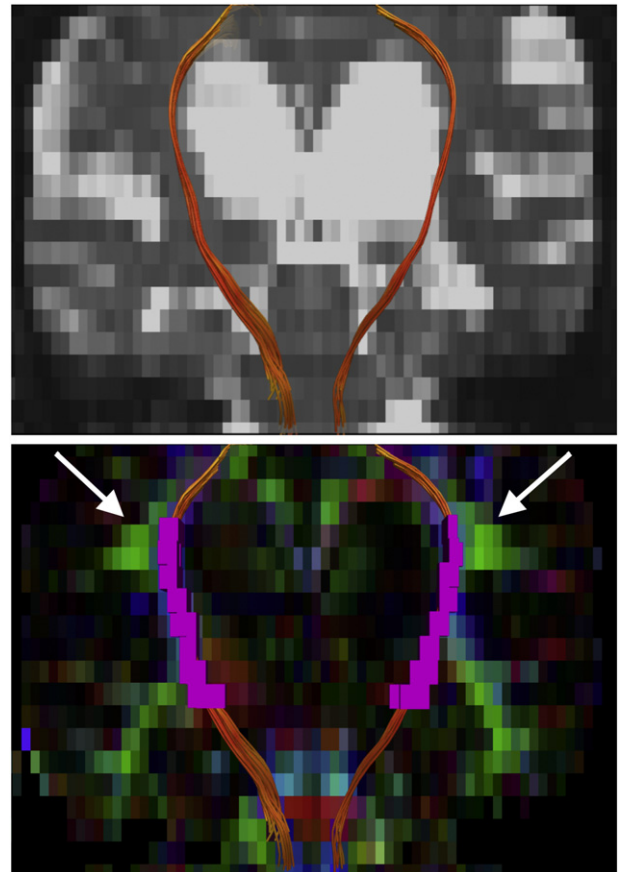

Fig. 2. An example of a volume of interest (VOI) for the tract-specific analyses. The CST tractography (orange) was voxelized, and the segment between the internal capsule and superior longitudinal fasciculus was used as the VOI (purple). The superior longitudinal fasciculus is shown as green (antero-posterior direction) on the color-coded FA map (arrows).
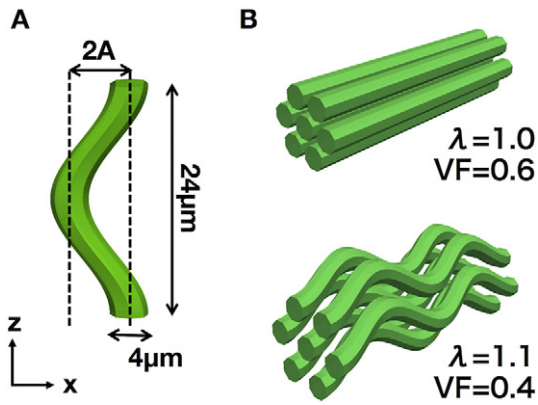
Fig. 3. Modelling of axon undulation. A. Each cylinder extends along the z direction and has a diameter of 4 μm. The cylinders undulate sinusoidally in the x direction (A = undulation amplitude). For consistency with a previous study (Nilsson et al., 2012), the strength of undulation is represented by λ (the ratio of the path length to the wavelength). λ is equal to 1 in a straight axon, and increases with undulation. B. The cylinders are hexagonally packed, with varying λ and axonal volume fraction (VF).

Each simulation consisted of 15,000 spins and 6000 time steps. The free diffusivity was set at 2.0×10^{-3} mm^2/s.

From the simulated random walks of particles, a virtual MRI signal was obtained using an acquisition scheme equivalent to that used for the human data. After the diffusion metrics were calculated, a variance-based sensitivity analysis (Skinner et al., 2015) was performed to quantify the effects of undulation and axonal volume fraction. A separate analysis of variance (ANOVA) was performed for each derived diffusion metric as the dependent variable, with λ and VF as factors. The sensitivity was defined as $S_i = SS_i/SS_{total}$, where SS_i is the partitioned sum of squares explained by factor i, and SS_{total} is the total sum of squares in the ANOVA. The specificity for either λ or VF was calculated as $S_\lambda - S_{VF}$, where a value of $+1$ indicates that the parameter was specific solely to undulation and a value of -1 indicates that it was specific solely to axonal volume fraction. Statistical analyses of both the clinical and simulation data were performed using R version 3.2.3 (R Foundation for Statistical Computing, Vienna, Austria. https://www.R-project.org/).

3. Results

3.1. Human data

In both NODDI and WMTI, τ_1 of the CST was significantly higher in the iNPH patients than in the controls (patients vs controls, 0.84 ± 0.02 vs 0.72 ± 0.04 in NODDI ($p < 0.001$), 0.80 ± 0.02 vs 0.76 ± 0.03 in WMTI ($p < 0.001$)) (Table 1 and Fig. 4), indicating a pathological increase of orientational coherence. After the surgery, τ_1 decreased significantly (Table 1 and Fig. 4). With NODDI, AWF of the CST was significantly lower in the patients than in the controls (0.53 ± 0.07 vs 0.63 ± 0.03 ($p = 0.002$)), but the difference did not reach significance with WMTI (0.48 ± 0.06 vs 0.53 ± 0.04 ($p = 0.06$)). No significant postoperative changes in AWF were observed with either NODDI or WMTI. The behaviors of τ_1 and AWF were consistent between NODDI and WMTI, although the estimated values varied between the two. The measures of parallel diffusivity (AD from DTI, and D_a and D_{epar} from WMTI) were higher in the patients than in the controls, and decreased after the surgery. FA also tended to be higher in the patients and decreased after the surgery as previously reported (Hattingen et al., 2010; Hattori et al., 2012; Jurcoane et al., 2014; Kim et al., 2011; Nakanishi et al., 2013; Scheel et al., 2012), although the differences were not significant in the present study.

3.2. Simulation

The simulation demonstrated that both NODDI and WMTI have the potential to disentangle the effects of axon stretching and axon density. AWF had high sensitivity and specificity for VF, and τ_1 had high sensitivity and specificity for λ (Table 2 and Fig. 5). As assessed visually, the effect of VF on τ_1 was relatively small to that of λ (Fig. 5), suggesting that the τ_1 changes observed in the patients reflect alteration of undulation/stretching, and is not much related to axon packing density. From WMTI, D_a was also specific to λ, whereas D_{epar} and D_{eperp} were more sensitive to VF than to λ. In DTI, FA and AD were sensitive to both VF and λ, whereas MD was sensitive almost solely to VF (Table 2 and Fig. 6).

4. Discussion

This study demonstrated that the increased orientational coherence of the CST in iNPH tends to normalize after CSF shunt surgery, whereas the decreased axon density remains unchanged. The observations of orientational coherence are consistent with the presumed axon stretching and its recovery. These findings were consistent in the two different models (NODDI and WMTI), although the estimated values varied between the two, as in a previous report (Jelescu et al., 2015). The ability of these methods to disentangle the effects of stretching and axon density was confirmed by the simulation experiment. The estimates of orientational coherence and axon density thus appear to serve as markers of reversible and irreversible changes in the CST of iNPH patients. The diffusion simulation experiment was useful for interpreting the clinical results. Recognition of how much the estimates of microstructural properties are affected by factors not explicitly considered by the model increased our confidence in the interpretation.

Table 1
Diffusion metrics of the corticospinal tract.

Metric	Controls	Patients before surgery (p value[a])	Patients after surgery (p value[b])
NODDI			
AWF	0.63 ± 0.03	0.53 ± 0.07 (0.002)[c]	0.54 ± 0.07 (0.47)
τ_1	0.72 ± 0.04	0.84 ± 0.02 (<0.001)[c]	0.80 ± 0.04 (0.001)[c]
WMTI			
AWF	0.53 ± 0.04	0.48 ± 0.06 (0.06)	0.49 ± 0.07 (0.86)
τ_1	0.76 ± 0.03	0.80 ± 0.02 (<0.001)[c]	0.77 ± 0.03 (0.01)[c]
D_a (10^{-3} mm^2/s)	1.09 ± 0.11	1.29 ± 0.11 (<0.001)[c]	1.22 ± 0.08 (0.03)[c]
D_{epar} (10^{-3} mm^2/s)	2.29 ± 0.19	2.55 ± 0.20 (0.004)[c]	2.38 ± 0.13 (<0.001)
D_{eperp} (10^{-3} mm^2/s)	0.81 ± 0.05	0.87 ± 0.11 (0.12)	0.90 ± 0.10 (0.30)
DTI			
FA	0.64 ± 0.03	0.67 ± 0.06 (0.22)	0.63 ± 0.06 (0.05)
AD (10^{-3} mm^2/s)	1.27 ± 0.08	1.53 ± 0.07 (<0.001)[c]	1.42 ± 0.10 (<0.001)[c]
RD (10^{-3} mm^2/s)	0.38 ± 0.03	0.44 ± 0.09 (0.08)	0.45 ± 0.09 (0.52)
MD (10^{-3} mm^2/s)	0.68 ± 0.03	0.80 ± 0.08 (<0.001)[c]	0.78 ± 0.08 (0.10)

[a] The preoperative values were compared with the controls using Welch's t-test.
[b] Changes in patient values before and after CSF shunt surgery were compared with paired t-tests.
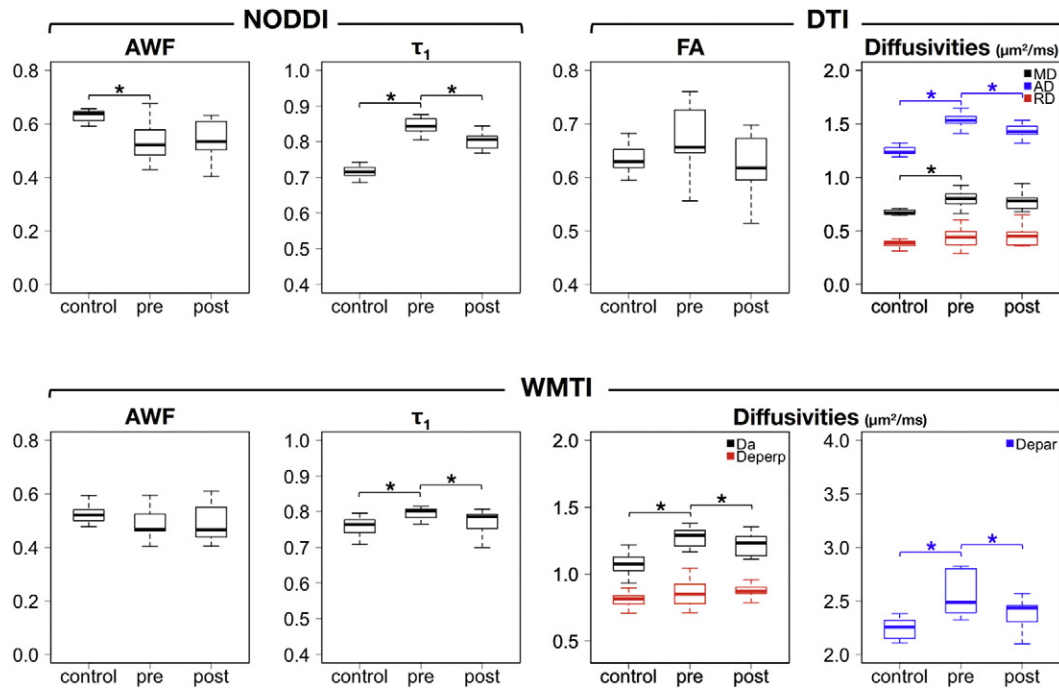[c] $p < 0.05$, significant.

Fig. 4. Box and whisker plots of the diffusion metrics in the normal control subjects and the iNPH patients before (pre) and after (post) surgery. Asterisks (*) indicate significant between-group differences. In both NODDI and WMTI, τ_1 was significantly higher in the preoperative patients than in the controls, indicating a pathological increase in orientational coherence, and tended to normalize after the surgery, indicating recovery. In NODDI, AWF was significantly lower in the patients than in the controls, which remained unchanged after the surgery. The behaviors of AWF and τ_1 were consistent between NODDI and WMTI, although the exact values differed between the two methods.

In addition, although NODDI and WMTI appeared able to estimate reversible and irreversible changes separately, MD derived from conventional DTI also seemed to reflect irreversible changes in the patients (Table 1) and was highly sensitive to axon density in the simulation (Table 2). Previous attempts have been made to predict treatment outcome using DTI (Jurcoane et al., 2014). Although FA and AD were not specific solely to stretching in the simulation, a multi-parametric classification scheme combined with MD may improve the predictive performance.

The present results may also facilitate the interpretation of previously reported findings. For example, using q-space diffusion displacement profiles, Hori et al. reported a postoperative increase in the root mean square displacement in the extra-axonal space (Hori et al., 2016). They focused on the diffusion perpendicular to the CST, and the present simulation result is compatible with their observation, in that recovery of physiological undulation (increase in λ) leads to an increase in D_{eperp} (Fig. 5). We speculate that the postoperative change in iNPH is a recovery of undulation, and not relief from dense packing by compaction, because Fig. 5 shows that decreasing VF cannot cause such postoperative decrease in τ_1 as observed in the present patient group.

It should be noted, though consistency between NODDI and WMTI as well as between the clinical data and simulation suggested axon undulation is a good candidate mechanism for the observed changes, we do not yet have conclusive evidence. Microscopically, non-straight, twisted or tortuous axon trajectories have been observed within the CST (Axer and Keyserlingk, 2000), and the tortuosity decreases with mechanical stretching (Hao and Shreiber, 2007), supporting the undulation/stretching hypothesis. However, undulation is very closely related to dispersion, and the effects from undulation and dispersion are considered indistinguishable by the method we used. Dispersion is almost ubiquitous within the brain even in the relatively coherent structures like internal capsule and corpus callosum (Axer et al., 2011; Budde and Annese, 2013). In the present study, comparison between the results from the human subjects (Fig. 4) and the simulation (Fig. 5) demonstrates that τ_1 in the normal subjects is lower than even the highest undulation in the simulation ($\lambda = 1.2$), indicating that undulation in

combination with dispersion may be a more complete and realistic scenario. Regarding other candidate sources of diffusion changes, the pathological findings in iNPH are nonspecific ischemia and gliosis (Akai et al., 1987; Del Bigio, 1993) that are associated with decreased FA. This implies increased axon density or myelination is unlikely as a source of the FA increase. Because iNPH is a disorder of CSF circulation, observation of the post-mortem brain may not be enough to detect the pathognomonic changes of the disease. Recently, increased FA and AD within the CST was reported also in Parkinson's disease and was interpreted as selective neurodegeneration or a compensatory increase in axon density (Mole et al., 2016). Our results indicate that the FA/AD increase in iNPH is based on a different mechanism, because the axon density was lower in iNPH than in the controls and did not show any changes that can be related to the partial normalization of FA/AD.

The present simulation experiment has some limitations. To the best of our knowledge, direct quantification of undulation amplitude in the human CST has not been reported. Therefore, we arbitrarily chose the axon radius and the scale of undulation to resemble those described by Nilsson et al. (2012). The microscopic, mesoscopic, and macroscopic

Table 2
Variance-based sensitivity analyses in the Monte-Carlo simulation.

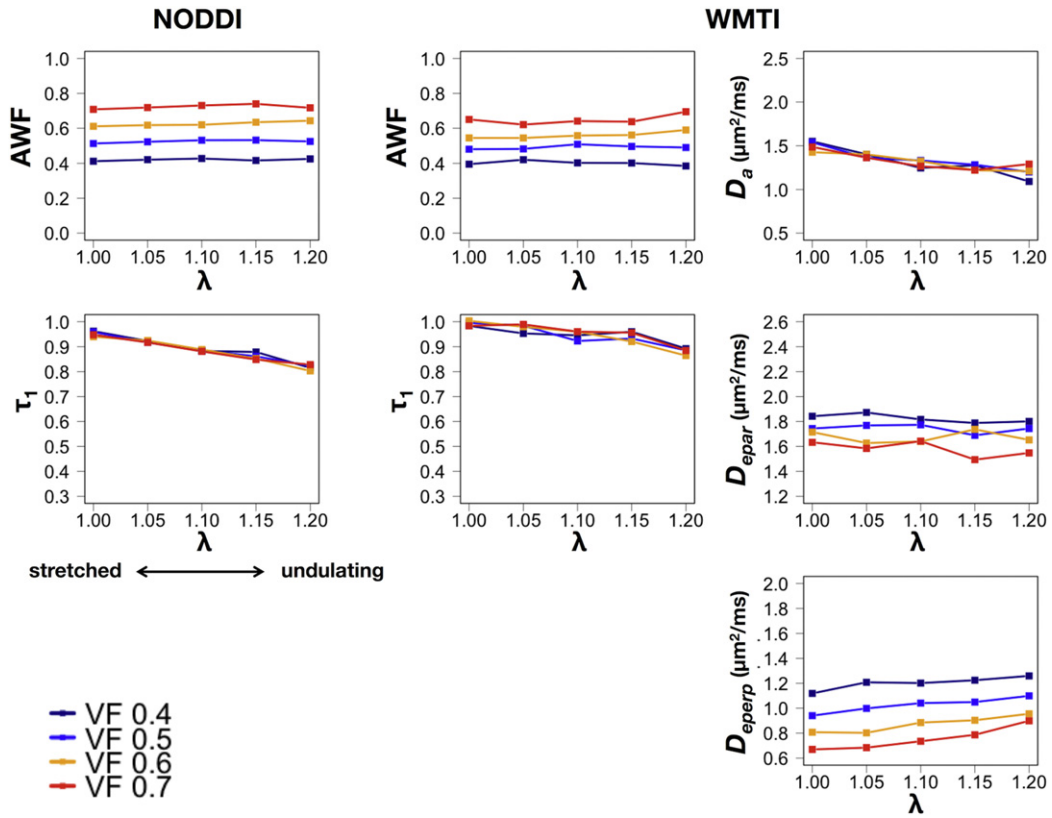| Metric	S_λ	S_{VF}	$S_\lambda - S_{VF}$
NODDI			
AWF	0.00	0.98	−0.98
τ_1	0.91	0.02	0.88
WMTI			
AWF	0.02	0.88	−0.86
τ_1	0.57	0.04	0.53
D_a	0.72	0.06	0.66
D_{epar}	0.09	0.43	−0.34
D_{eperp}	0.08	0.84	−0.76
DTI			
FA	0.31	0.67	−0.36
AD	0.62	0.33	0.29
RD	0.07	0.92	−0.85
MD	0.01	0.97	−0.96

Fig. 5. Simulated effects of undulation (λ) and axonal volume fraction (VF) on the NODDI and WMTI metrics.

scales of undulation affect diffusivities, and probably NODDI and WMTI metrics, to different degrees (Nilsson et al., 2012). Also, the experiment was conducted in the absence of complex features, such as fiber crossing and heterogeneity in axon diameter and packing density. The undulation was also modeled in a simplified way, in that all axons had a coherent and constant degree of undulation along the entire tract. Complex geometry, such as fiber crossings, may considerably decrease the sensitivity and specificity of the estimated parameters to the microstructural properties of interest (Skinner et al., 2015).

This study had several other limitations. First, we were unable to correlate our imaging findings with symptom severity or treatment outcome, as only a small number of patients were involved and all of them reported postoperative improvements in gait. Second, the present data do not cover the whole brain, although iNPH is associated with widespread microstructural alterations in the brain (Hattori et al., 2012; Jurcoane et al., 2014; Scheel et al., 2012). Also, the spatial resolution in the slice direction is low as a trade-off to gain the in-plane resolution and signal-to-noise ratio in a clinically achievable scan time, and
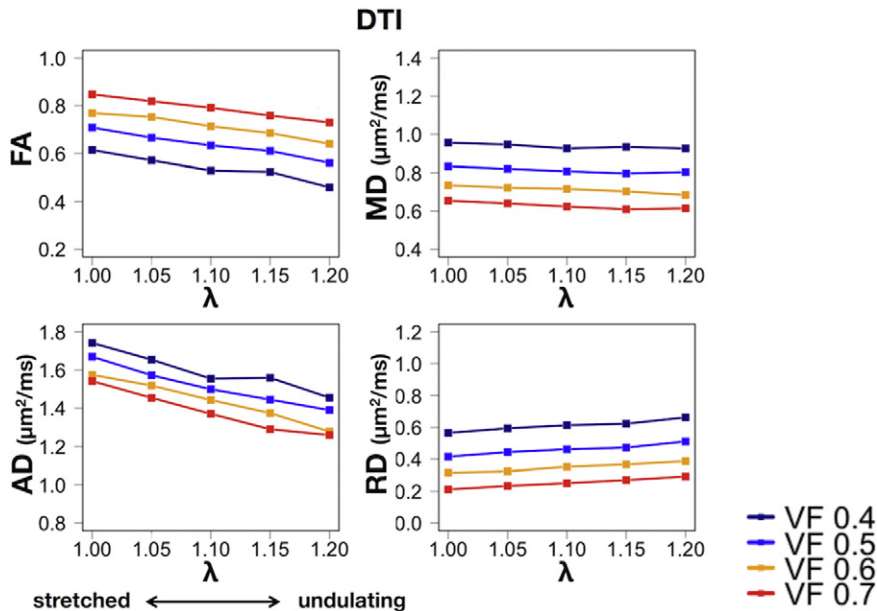

Fig. 6. Simulated effects of undulation (λ) and axonal volume fraction (VF) on the DTI metrics.

hence partial volume effects could be high in this data set. Lastly, solving the intrinsic limitations of NODDI and WMTI is beyond the scope of this study. Although consistency between the clinical data and simulation supported our hypothesis of undulation/stretching, the results still need to be interpreted with caution. Towards a parameter estimation that do not rely on specific fiber orientation, there are emerging approaches that use the rotation invariant (RotInv) feature, including spherical mean technique (Kaden et al., 2016), LEMONADE (Novikov et al., 2016b), and Bayesian RotInv framework (Reisert et al., 2017). Another promising direction is to incorporate the time-dependency of diffusion in the extra-axonal space for more precise quantification in the presence of complex features like beading, undulation, and heterogeneity of axon geometry (De Santis et al., 2016; Fieremans et al., 2016). Recently, Ning et al. proposed PICASO model (Ning et al., 2017) that captures structural organization with consideration of the time-dependent diffusion by introducing the diffusion disturbance function. The rapid progress in diffusion microstructural imaging is expected to yield deeper insights into the white matter alterations of iNPH in the near future.

5. Conclusion

The pathologically high orientational coherence within the CST in iNPH tends to normalize after shunt surgery, which can be interpreted as recovery from axon stretching. The estimated axon density was lower in iNPH than in controls and remained unchanged after the surgery, suggesting its potential role as a marker of chronic and irreversible neuronal damage. Thus, the present results suggest that diffusion MRI can distinguish between reversible and irreversible changes in iNPH, bringing us closer to a quantitative image biomarker that can predict treatment outcome. As a next step, we are planning a prospective study to investigate the correlations with symptoms and treatment outcome in a larger cohort.

Disclosure statement

The authors have no actual or potential conflicts of interest.

Acknowledgement

References

Abe, O., Aoki, S., Hayashi, N., Yamada, H., Kunimatsu, A., Mori, H., Yoshikawa, T., Okubo, T., Ohtomo, K., 2002. Normal aging in the central nervous system: quantitative MR diffusion-tensor analysis. Neurobiol. Aging 23, 433–441.

Akai, K., Uchigasaki, S., Tanaka, U., Komatsu, A., 1987. Normal pressure hydrocephalus. Neuropathological study. Acta Pathol. Jpn. 37, 97–110.

Alexander, D.C., Hubbard, P.L., Hall, M.G., Moore, E.A., Ptito, M., Parker, G.J.M., Dyrby, T.B., 2010. Orientationally invariant indices of axon diameter and density from diffusion MRI. NeuroImage 52, 1374–1389.

Andersson, J.L.R., Sotiropoulos, S.N., 2016. An integrated approach to correction for off-resonance effects and subject movement in diffusion MR imaging. NeuroImage 125, 1063–1078.

Assaf, Y., Basser, P.J., 2005. Composite hindered and restricted model of diffusion (CHARMED) MR imaging of the human brain. NeuroImage 27, 48–58.

Axer, H., Keyserlingk, D.G., 2000. Mapping of fiber orientation in human internal capsule by means of polarized light and confocal scanning laser microscopy. J. Neurosci. Methods 94, 165–175.

Axer, H., Beck, S., Axer, M., Schuchardt, F., Heepe, J., Flücken, A., Axer, M., Prescher, A., Witte, O.W., 2011. Microstructural analysis of human white matter architecture using polarized light imaging: views from neuroanatomy. Front. Neuroinform. 5, 28.

Bradley, W.G., 2015. CSF flow in the brain in the context of normal pressure hydrocephalus. AJNR Am. J. Neuroradiol. 36, 831–838.

Brandstack, N., Kurki, T., Laalo, J., Kauko, T., Tenovuo, O., 2016. Reproducibility of tract-based and region-of-interest DTI analysis of long association tracts. Clin. Neuroradiol. 26, 199–208.

Budde, M.D., Annese, J., 2013. Quantification of anisotropy and fiber orientation in human brain histological sections. Front. Integr. Neurosci. 7, 3.

Burcaw, L.M., Fieremans, E., Novikov, D.S., 2015. Mesoscopic structure of neuronal tracts from time-dependent diffusion. NeuroImage 114, 18–37.

Cercignani, M., Giulietti, G., Dowell, N.G., Gabel, M., 2017. Characterizing axonal myelination within the healthy population: a tract-by-tract mapping of effects of age and gender on the fiber g-ratio. Neurobiol. Aging 49, 109–118.

Cohen, Y., Anaby, D., Morozov, D., 2017. Diffusion MRI of the spinal cord: from structural studies to pathology. NMR Biomed. 30, e3592. http://dx.doi.org/10.1002/nbm.3592.

Colgan, N., Siow, B., O'Callaghan, J.M., Harrison, I.F., Wells, J.A., Holmes, H.E., Ismail, O., Richardson, S., Alexander, D.C., Collins, E.C., Fisher, E.M., Johnson, R., Schwarz, A.J., Ahmed, Z., O'Neill, M.J., Murray, T.K., Zhang, H., Lythgoe, M.F., 2015. Application of neurite orientation dispersion and density imaging (NODDI) to a tau pathology model of Alzheimer's disease. NeuroImage 125, 739–744.

De Santis, S., Jones, D.K., Roebroeck, A., 2016. Including diffusion time dependence in the extra-axonal space improves in vivo estimates of axonal diameter and density in human white matter. NeuroImage 130, 91–103.

Del Bigio, M.R., 1993. Neuropathological changes caused by hydrocephalus. Acta Neuropathol. 85, 573–585.

Fieremans, E., Jensen, J.H., Helpern, J.A., 2011. White matter characterization with diffusional kurtosis imaging. NeuroImage 58, 177–188.

Fieremans, E., Burcaw, L.M., Lee, H.-H., Lemberskiy, G., Veraart, J., Novikov, D.S., 2016. In vivo observation and biophysical interpretation of time-dependent diffusion in human white matter. NeuroImage 129, 414–427.

Glenn, G.R., Helpern, J.A., Tabesh, A., Jensen, J.H., 2015. Optimization of white matter fiber tractography with diffusional kurtosis imaging. NMR Biomed. 28, 1245–1256.

Hall, M.G., Alexander, D.C., 2009. Convergence and parameter choice for Monte-Carlo simulations of diffusion MRI. IEEE Trans. Med. Imaging 28, 1354–1364.

Halperin, J.J., Kurlan, R., Schwalb, J.M., Cusimano, M.D., Gronseth, G., Gloss, D., 2015. Practice guideline: idiopathic normal pressure hydrocephalus: response to shunting and predictors of response: report of the guideline development, dissemination, and implementation subcommittee of the American Academy of neurology. Neurology 85, 2063–2071.

Hao, H., Shreiber, D.I., 2007. Axon kinematics change during growth and development. J. Biomech. Eng. 129, 511–522.

Hattingen, E., Jurcoane, A., Melber, J., Blasel, S., Zanella, F.E., Neumann-Haefelin, T., Singer, O.C., 2010. Diffusion tensor imaging in patients with adult chronic idiopathic hydrocephalus. Neurosurgery 66, 917–924.

Hattori, T., Ito, K., Aoki, S., Yuasa, T., Sato, R., Ishikawa, M., Sawaura, H., Hori, M., Mizusawa, H., 2012. White matter alteration in idiopathic normal pressure hydrocephalus: tract-based spatial statistics study. AJNR Am. J. Neuroradiol. 33, 97–103.

Hori, M., Kamiya, K., Nakanishi, A., Fukunaga, I., Miyajima, M., Nakajima, M., Suzuki, M., Suzuki, Y., Irie, R., Kamagata, K., Arai, H., Aoki, S., 2016. Prospective estimation of mean axon diameter and extra-axonal space of the posterior limb of the internal capsule in patients with idiopathic normal pressure hydrocephalus before and after a lumboperitoneal shunt by using q-space diffusion MRI. Eur. Radiol. 26, 2992–2998.

Irie, R., Tsuruta, K., Hori, M., Suzuki, M., Kamagata, K., Nakanishi, A., Kamiya, K., Nakajima, M., Miyajima, M., Arai, H., Aoki, S., 2017. Neurite orientation dispersion and density imaging for evaluation of corticospinal tract in idiopathic normal pressure hydrocephalus. Jpn. J. Radiol. 35, 25–30.

Jelescu, I.O., Veraart, J., Adisetiyo, V., Milla, S.S., Novikov, D.S., Fieremans, E., 2015. One diffusion acquisition and different white matter models: how does microstructure change in human early development based on WMTI and NODDI? NeuroImage 107, 242–256.

Jensen, J.H., Helpern, J.A., 2010. MRI quantification of non-Gaussian water diffusion by kurtosis analysis. NMR Biomed. 23, 698–710.

Jeurissen, B., Tournier, J.-D., Dhollander, T., Connelly, A., Sijbers, J., 2014. Multi-tissue constrained spherical deconvolution for improved analysis of multi-shell diffusion MRI data. NeuroImage 103, 411–426.

Jones, D.K., Knösche, T.R., Turner, R., 2013. White matter integrity, fiber count, and other fallacies: the do's and don'ts of diffusion MRI. NeuroImage 73, 239–254.

Jurcoane, A., Keil, F., Szelenyi, A., Pfeilschifter, W., Singer, O.C., Hattingen, E., 2014. Directional diffusion of corticospinal tract supports therapy decisions in idiopathic normal-pressure hydrocephalus. Neuroradiology 56, 5–13.

Kaden, E., Kelm, N.D., Carson, R.P., Does, M.D., Alexander, D.C., 2016. Multi-compartment microscopic diffusion imaging. NeuroImage 139, 346–359.

Kamagata, K., Hatano, T., Okuzumi, A., Motoi, Y., Abe, O., Shimoji, K., Kamiya, K., Suzuki, M., Hori, M., Kumamaru, K.K., Hattori, N., Aoki, S., 2016. Neurite orientation dispersion and density imaging in the substantia nigra in idiopathic Parkinson disease. Eur. Radiol. 26, 2567–2577.

Kazui, H., Miyajima, M., Mori, E., Ishikawa, M., SINPHONI-2 Investigators, 2015. Lumboperitoneal shunt surgery for idiopathic normal pressure hydrocephalus (SINPHONI-2): an open-label randomised trial. Lancet Neurol. 14, 585–594.

Kim, M.J., Seo, S.W., Lee, K.M., Kim, S.T., Lee, J.I., Nam, D.H., Na, D.L., 2011. Differential diagnosis of idiopathic normal pressure hydrocephalus from other dementias using diffusion tensor imaging. AJNR Am. J. Neuroradiol. 32, 1496–1503.

Merluzzi, A.P., Dean, D.C., Adluru, N., Suryawanshi, G.S., Okonkwo, O.C., Oh, J.M., Hermann, B.P., Sager, M.A., Asthana, S., Zhang, H., Johnson, S.C., Alexander, A.L., Bendlin, B.B., 2016. Age-dependent differences in brain tissue microstructure assessed with neurite orientation dispersion and density imaging. Neurobiol. Aging 43, 79–88.

Miyajima, M., Kazui, H., Mori, E., Ishikawa, M., on behalf of the SINPHONI-2 Investigators, 2016. One-year outcome in patients with idiopathic normal-pressure hydrocephalus: comparison of lumboperitoneal shunt to ventriculoperitoneal shunt. J. Neurosurg. 1–10.

Mole, J.P., Subramanian, L., Bracht, T., Morris, H., Metzler-Baddeley, C., Linden, D.E.J., 2016. Increased fractional anisotropy in the motor tracts of Parkinson's disease suggests

compensatory neuroplasticity or selective neurodegeneration. Eur. Radiol. 26, 3327–3335.

Mori, E., Ishikawa, M., Kato, T., Kazui, H., Miyake, H., Miyajima, M., Nakajima, M., Hashimoto, M., Kuriyama, N., Tokuda, T., Ishii, K., Kaijima, M., Hirata, Y., Saito, M., Arai, H., Japanese Society of Normal Pressure Hydrocephalus, 2012. Guidelines for management of idiopathic normal pressure hydrocephalus: second edition. Neurol. Med. Chir. (Tokyo) 52, 775–809.

Nakanishi, A., Fukunaga, I., Hori, M., Masutani, Y., Takaaki, H., Miyajima, M., Aoki, S., 2013. Microstructural changes of the corticospinal tract in idiopathic normal pressure hydrocephalus: a comparison of diffusion tensor and diffusional kurtosis imaging. Neuroradiology 55, 971–976.

Nilsson, M., Lätt, J., Ståhlberg, F., van Westen, D., Hagslätt, H., 2012. The importance of axonal undulation in diffusion MR measurements: a Monte Carlo simulation study. NMR Biomed. 25, 795–805.

Ning, L., Özarslan, E., Westin, C.-F., Rathi, Y., 2017. Precise Inference and Characterization of Structural Organization (PICASO) of tissue from molecular diffusion. NeuroImage 146, 452–473.

Novikov, D.S., Jespersen, S.N., Kiselev, V.G., Fieremans, E., 2016a. Quantifying brain microstructure with diffusion MRI: theory and parameter estimation (eprint arXiv: 1609.09144).

Novikov, D.S., Veraart, J., Jelescu, I.O., Fieremans, E., 2016b. Mapping orientational and microstructural metrics of neuronal integrity with in vivo diffusion MRI (eprint arXiv: 1609.09144).

Poca, M.A., Mataró, M., Matarín, M., Arikan, F., Junqué, C., Sahuquillo, J., 2005. Good outcome in patients with normal-pressure hydrocephalus and factors indicating poor prognosis. J. Neurosurg. 103, 455–463.

Reisert, M., Kellner, E., Dhital, B., Hennig, J., Kiselev, V.G., 2017. Disentangling micro from mesostructure by diffusion MRI: a Bayesian approach. NeuroImage 147, 964–975.

Ringstad, G., Emblem, K.E., Eide, P.K., 2016. Phase-contrast magnetic resonance imaging reveals net retrograde aqueductal flow in idiopathic normal pressure hydrocephalus. J. Neurosurg. 124, 1850–1857.

Scheel, M., Diekhoff, T., Sprung, C., Hoffmann, K.-T., 2012. Diffusion tensor imaging in hydrocephalus—findings before and after shunt surgery. Acta Neurochir. 154, 1699–1706.

Sexton, C.E., Kalu, U.G., Filippini, N., Mackay, C.E., Ebmeier, K.P., 2011. A meta-analysis of diffusion tensor imaging in mild cognitive impairment and Alzheimer's disease. Neurobiol. Aging 32, 2322, e5–18.

Shizukuishi, T., Abe, O., Aoki, S., 2013. Diffusion tensor imaging analysis for psychiatric disorders. Magn. Reson. Med. Sci. 12, 153–159.

Skinner, N.P., Kurpad, S.N., Schmit, B.D., Budde, M.D., 2015. Detection of acute nervous system injury with advanced diffusion-weighted MRI: a simulation and sensitivity analysis. NMR Biomed. 28, 1489–1506.

Solana, E., Sahuquillo, J., Junqué, C., Quintana, M., Poca, M.A., 2012. Cognitive disturbances and neuropsychological changes after surgical treatment in a cohort of 185 patients with idiopathic normal pressure hydrocephalus. Arch. Clin. Neuropsychol. 27, 304–317.

Tustison, N.J., Avants, B.B., Cook, P.A., Zheng, Y., Egan, A., Yushkevich, P.A., Gee, J.C., 2010. N4ITK: improved N3 bias correction. IEEE Trans. Med. Imaging 29, 1310–1320.

Veraart, J., Poot, D.H.J., Van Hecke, W., Blockx, I., Van der Linden, A., Verhoye, M., Sijbers, J., 2011. More accurate estimation of diffusion tensor parameters using diffusion kurtosis imaging. Magn. Reson. Med. 65, 138–145.

Veraart, J., Sijbers, J., Sunaert, S., Leemans, A., Jeurissen, B., 2013. Weighted linear least squares estimation of diffusion MRI parameters: strengths, limitations, and pitfalls. NeuroImage 81, 335–346.

Veraart, J., Fieremans, E., Novikov, D.S., 2016. Diffusion MRI noise mapping using random matrix theory. Magn. Reson. Med. 76, 1582–1593.

Virhammar, J., Laurell, K., Cesarini, K.G., Larsson, E.-M., 2014. Preoperative prognostic value of MRI findings in 108 patients with idiopathic normal pressure hydrocephalus. AJNR Am. J. Neuroradiol. 35, 2311–2318.

Wakana, S., Caprihan, A., Panzenboeck, M.M., Fallon, J.H., Perry, M., Gollub, R.L., Hua, K., Zhang, J., Jiang, H., Dubey, P., Blitz, A., van Zijl, P., Mori, S., 2007. Reproducibility of quantitative tractography methods applied to cerebral white matter. NeuroImage 36, 630–644.

Zhang, H., Schneider, T., Wheeler-Kingshott, C.A., Alexander, D.C., 2012. NODDI: practical in vivo neurite orientation dispersion and density imaging of the human brain. NeuroImage 61, 1000–1016.